



## CO oxidation by Pd supported on CeO<sub>2</sub>(100) and CeO<sub>2</sub>(111) facets

Giulia Spezzati<sup>a</sup>, Angelica D. Benavidez<sup>b</sup>, Andrew T. DeLaRiva<sup>b</sup>, Yaqiong Su<sup>a</sup>, Jan P. Hofmann<sup>a</sup>, Shunsuke Asahina<sup>c</sup>, Ezra J. Olivier<sup>d</sup>, Johannes H. Neethling<sup>d</sup>, Jeffrey T. Miller<sup>e</sup>, Abhaya K. Datye<sup>b,\*</sup>, Emiel J.M. Hensen<sup>a,\*</sup>



<sup>a</sup> Laboratory of Inorganic Materials Chemistry, Department of Chemical Engineering and Chemistry, Eindhoven University of Technology, P.O. Box 513, 5600 MB Eindhoven, the Netherlands

<sup>b</sup> Department of Chemical & Biological Engineering and Center for Microengineered Materials, University of New Mexico, Albuquerque, NM 87131, USA

<sup>c</sup> SM Application Group, JEOL Ltd., Akisima, Tokyo 196-8558, Japan

<sup>d</sup> Center for High Resolution Transmission Electron Microscopy, Physics Department, Nelson Mandela University, Port Elizabeth, 6031, South Africa

<sup>e</sup> Davidson School of Chemical Engineering, Purdue University, West Lafayette, IN 47907, USA

### ARTICLE INFO

#### Keywords:

CeO<sub>2</sub>  
Palladium  
CO oxidation  
Reaction mechanism  
Single atoms

### ABSTRACT

Pd/CeO<sub>2</sub> is an active component in emission control catalysts for CO oxidation. Nanostructured CeO<sub>2</sub> powders can be prepared in the form of rods exposing predominantly (111) surfaces and cubes exposing (100) surfaces. While differences in the reactivity of Pd supported on these facets of ceria have been reported, the origins of the reactivity differences are not well understood. Pd supported on (111) surfaces of ceria rods exhibits room-temperature CO oxidation activity, while Pd on (100) surface of ceria cubes shows comparable activity at a temperature that is 60 °C higher. Earlier, we established that Pd/CeO<sub>2</sub>-rods are active due to a Langmuir-Hinshelwood mechanism involving isolated Pd atoms in the form of Pd<sub>1</sub>O and Pd<sub>1</sub>O<sub>2</sub> species. Here, we establish using *in situ* CO IR spectroscopy and density functional theory (DFT) that, in addition to TEM-visible Pd nanoparticles, Pd/CeO<sub>2</sub>-cubes also contain isolated Pd species, predominantly in the form of Pd<sub>1</sub>O. DFT calculations show that CO oxidation proceeds via a Mars-van Krevelen pathway, which is possible for the (100) surface because of the lower Ce-O binding energy compared to the (111) surface. Overall, the catalytic cycle for CO oxidation on Pd/CeO<sub>2</sub>(100) involves a higher free energy barrier than on Pd/CeO<sub>2</sub>(111) in keeping with the experimentally observed activity difference. EXAFS measurements show that the active Pd phase in both Pd/CeO<sub>2</sub>-rods and Pd/CeO<sub>2</sub>-cubes responds dynamically with respect to reducing and oxidizing conditions. The redisposition of Pd in oxidative conditions is more pronounced for Pd/CeO<sub>2</sub>-rods and the catalyst is more active after an oxidative treatment.

### 1. Introduction

Cerium dioxide (CeO<sub>2</sub>) is a versatile compound used in a wide variety of technological applications, such as in oxygen sensors [1], solid-oxide fuel cells (SOFC) [2], catalysis and other key areas [3]. Its most important application in catalysis is as a support for noble metals in three-way catalysis (TWC) [4]. An important property of ceria is that it can reversibly change the Ce oxidation state from + 4 to + 3 when oxygen atoms are removed from the ceria surface. This oxygen storage capacity (OSC) is used in TWC technology to retain oxidation activity under fuel-rich conditions [5,6].

In the last decade, there have been substantial efforts to understand the facet-dependent chemical reactivity of CeO<sub>2</sub> surfaces. The use of well-defined CeO<sub>2</sub> nanostructures can lead to improved catalytic

performance [7–9]. A variety of preparation methods such as hydrothermal synthesis [10], liquid precipitation [11], and solvothermal procedures [12] have been used to obtain specific morphologies of ceria such as octahedra, nanorods, nanowires, nanospheres and nanocubes. With these anisotropic CeO<sub>2</sub> nanomaterials, a deeper understanding can be gained about the interaction of specific surface facets with transition metals and their impact on catalytic activity. CeO<sub>2</sub> crystallizes in the fluorite structure and the most stable surface terminations are the (111), (110) and (100) facets. The (111) surface consists of both Ce and O atoms in a single plane while the polar (110) and the (100) surfaces are corrugated and expose either Ce or O atoms [13]. The most stable surface is (111) terminated, followed by (110) and (100) terminations [14]. Low surface area nanoparticles obtained in high-temperature processes and nano-sized octahedra preferentially expose the (111)

\* Corresponding authors.

E-mail addresses: [datye@unm.edu](mailto:datye@unm.edu) (A.K. Datye), [E.J.M.Hensen@tue.nl](mailto:E.J.M.Hensen@tue.nl) (E.J.M. Hensen).

surface, while nanocubes mainly expose the (100) surface [15]. There remains a considerable debate about the surface exposed by nanorods. Initially, it was claimed that nanorods predominantly expose the (110) surface [16], but a detailed aberration-corrected TEM investigation and comparison of the specific reactivity of rods and octahedra for the water-gas shift (WGS) reaction demonstrated that the dominant surface termination is the (111) surface along with some exposed (100) facets [17]. A recent study using infrared reflection absorption spectroscopy confirmed that ceria rods are mainly enclosed by (111) facets [18], especially when the rods have been annealed at elevated temperatures.

There is substantial agreement in literature about the role of oxygen vacancies for achieving high catalytic performance in oxidation reactions, such as CO oxidation [19,20]. The presence of oxygen vacancies may indicate a direct involvement of surface CeO<sub>2</sub> oxygen atoms in the catalytic cycle [21,22]. The energy required to form oxygen vacancies is lower on (100) facets, compared to the (111) or (110) ones, which makes CeO<sub>2</sub>(100) the most reducible ceria surface [23]. Surface science model studies have demonstrated that it is difficult to reduce the CeO<sub>2</sub>(111) and CeO<sub>2</sub>(100) surfaces [24,25], suggesting that defects or nanoscale effects in ceria powders are important aspects. One of the most attractive features of CeO<sub>2</sub> is the ability to stabilize noble metal particles, clusters and even single atoms on its surface [26]. The high reactivity of the CeO<sub>2</sub> surface and the presence of vacancies in combination with noble metal species make these systems highly active in a number of catalyzed reactions, such as CO oxidation, NO<sub>x</sub> reduction and CH<sub>4</sub> oxidation [5,27,28]. Pd is increasingly used in these applications because of its lower cost compared to other noble metals. A variety of methods have been used to deposit Pd onto the CeO<sub>2</sub> surface, such as wet impregnation [29] and deposition-precipitation [30]. The influence of the Pd loading and the preparation method on the final catalytic performance in CO oxidation has also been studied [31–33]. Specifically, there is evidence of PdO clusters and single atoms being more active for CO oxidation than reduced Pd nanoparticles [5,34–36]. The work of Cagnello et al. has clearly shown how CO oxidation takes place on the active sites at the interface between CeO<sub>2</sub> and Pd nanoparticles, thus substantiating the role of metal-support interaction [37]. Moreover, due to strong metal-support interaction ceria-supported catalysts are known to exhibit high thermal stability against sintering [26].

Due to the difficulty of synthesizing well-defined facets in oxide supports, there are relatively few investigations of the role of specific facets on the reactivity of the supported metal. The ease of synthesis of faceted ceria nanoshapes (rods, cubes and octahedra) makes it possible to study facet-dependent reactivity. For instance, a comparison of single atoms and clusters of gold on different CeO<sub>2</sub> nanostructures showed that Au/CeO<sub>2</sub> nanorods displayed a stronger Au-CeO<sub>2</sub> interaction and a higher activity in the WGS reaction than cube- and polyhedra-shaped CeO<sub>2</sub> [38]. Peng et al. studied the performance of Pd on different CeO<sub>2</sub> nanostructures in toluene oxidation and concluded that nanorod CeO<sub>2</sub> led to the highest activity due to a high concentration of surface vacancies [39]. Soler et al. used CO oxidation and CO preferential oxidation to compare the catalytic performance of nanostructured Au/CeO<sub>2</sub> materials. Also in this case, the highest activity was observed for the nanorod-shaped samples. It was suggested that the occurrence of oxidized Au and Ce<sup>3+</sup> species is related to a strong metal-support interaction. Conversely, it was suggested that oxidized species that strongly interact with the support were absent in cubes and polyhedra-shaped samples [40].

As Pd is known to undergo facile oxidation and reduction, we evaluated in the present study the facet-dependent redox behavior of Pd and the catalytic performance in CO oxidation. We studied catalysts comprised of 1 wt% Pd deposited on nanorod and nanocube forms of ceria, whose surfaces are dominated by (111) and (100) terminations, respectively. The nanorod-shaped sample has already been characterized in a previous publication [41]. Here, we follow a similar approach combining HR-TEM, *in situ* CO IR spectroscopy and computational DFT

modeling to follow the speciation of Pd on the nanocube surface in comparison to nanorod based catalysts. We also use DFT to compute a reaction mechanism for CO oxidation on the nanocube sample and use microkinetics simulations to confirm that the nanorod sample should be more active than the nanocube one. A major result presented in this work is that nanocube ceria-supported Pd also contains isolated Pd atoms in addition to TEM-observable nanoparticles, but their specific geometry makes the isolated Pd atoms inactive at room temperature. The dynamics of nanorod and nanocube ceria supported Pd active phases are investigated by *in situ* EXAFS.

## 2. Experimental

### 2.1. Catalyst preparation

Ce(NO<sub>3</sub>)<sub>3</sub>·6H<sub>2</sub>O (99.5% purity) was purchased from Alfa Aesar. Pd (NO<sub>3</sub>)<sub>2</sub>·2H<sub>2</sub>O (40% Pd basis), NaOH (reagent grade, ≥98%) were purchased from Sigma Aldrich. Absolute ethanol (99.5% purity) was purchased from VWR. Sipernat® 50 high surface silica was purchased from Evonik. All compounds were used without further purification.

The synthesis of the CeO<sub>2</sub> nanorods and nanocubes was performed via a hydrothermal method adapted from Mai et al. [10]. An aliquot of 5 mL of an aqueous 5 mM Ce(NO<sub>3</sub>)<sub>3</sub>·6H<sub>2</sub>O solution was added to 35 mL of a 17.1 M solution of NaOH. For both solutions, deionized water was employed. The resulting slurry was stirred at room temperature for 1 h, and afterwards diluted to a final volume of 100 mL. The mixture was poured in a 125 mL Teflon liner, which was inserted in a stainless-steel autoclave. The hydrothermal treatment was conducted in an oven. In order to obtain CeO<sub>2</sub> nanorods, the mixture was treated at 100 °C for 24 h under static conditions. CeO<sub>2</sub> nanocubes were obtained at a temperature of 180 °C using tumbling at 80 rpm for 24 h. Tumbling resulted in a more uniform size of the nanocubes. After hydrothermal treatment, the autoclaves were quickly quenched in a water bath. The solid products were separated from the liquid by centrifugation, washed four times with deionized water and twice with ethanol. CeO<sub>2</sub> was dried at 80 °C in a vacuum oven for 2 h and then calcined at 500 °C for 4 h in a gas flow composed of 80 mL/min of He and 20 mL/min of O<sub>2</sub>. The samples are called CeO<sub>2</sub>-rod and CeO<sub>2</sub>-cube, respectively.

Palladium nanoparticles were deposited on the CeO<sub>2</sub> supports by means of a wet impregnation technique. Pd(NO<sub>3</sub>)<sub>2</sub>·2H<sub>2</sub>O was dissolved in deionized water and the resulting solution was used to impregnate the solid. The mixture was stirred for 30 min and the water was slowly evaporated by heating the solution while stirring. The solid was dried at 110 °C and calcined at 300 °C for 4 h in a gas flow composed of 80 mL/min of He and 20 mL/min of O<sub>2</sub>. The final Pd loading was 1 wt%. A similar approach was used to impregnate 5% weight of Pd on the silica support as well, as a reference sample. For the sake of simplicity, the sample with 1 wt% of palladium deposited on CeO<sub>2</sub> nanorods is labelled as Pd/CeO<sub>2</sub>-rod, while the sample with 1% wt% palladium on CeO<sub>2</sub> nanocubes is labelled as Pd/CeO<sub>2</sub>-cube. The silica-based sample is labelled Pd/SiO<sub>2</sub>.

### 2.2. Catalyst characterization

XRD patterns were recorded on a Bruker D2 Phaser powder diffraction system using Cu K $\alpha$  radiation with a time per step of 0.5 min and a step size of 0.02° in the range 10–90 ° 2 $\theta$ .

N<sub>2</sub> physisorption was performed at –196 °C on a TriStar II 3020 instrument. Typically, 200 mg of sample were transferred into a home-made glass sample holder. The pretreatment involved heating to 120 °C under a N<sub>2</sub> flow overnight to allow for desorption of water and impurities. The Brunauer-Emmet-Teller (BET) method was used to calculate the surface area.

The Pd loading was determined using a ICP-OES instrument (Spectroblue, AMETEK Inc.). Typically, 50 mg of sample was dissolved in 5 mL concentrated H<sub>2</sub>SO<sub>4</sub>. The mixture was stirred and heated at

150 °C until the sample was fully solubilized. The wavelengths used for Pd determination were 324.270 nm and 340.458 nm.

High-resolution low-voltage SEM measurements were performed on a JSM-7800 F instrument at JEOL (Japan). TEM measurements were performed on a FEI Tecnai 20 electron microscope at an electron acceleration voltage of 200 kV with a LaB<sub>6</sub> filament. Additionally, we used a JEOL 2010 F and an aberration-corrected ARM 200 F for observation of the samples at higher magnification. A suitable quantity of powder was dispersed in ethanol, sonicated and deposited on a carbon-coated Cu grid. Particle counting was performed with the software ImageJ, counting at least 100 particles.

Infrared spectra were recorded on a Bruker Vertex 70v FTIR spectrometer equipped with a DTGS detector. The experiments were performed *in situ* by using a home-built environmental transmission IR cell. The background was collected in an empty cell by averaging 512 scans with a resolution of 2 cm<sup>-1</sup> in the 4000–1000 cm<sup>-1</sup> range. Self-supporting pellets were made by pressing approximately 20 mg of a sample in a disk with a diameter of 13 mm. Each spectrum was collected by averaging 32 scans with a resolution of 2 cm<sup>-1</sup> in the 4000–1000 cm<sup>-1</sup> range. The samples were either oxidized or reduced before *in situ* IR investigations. For oxidation, the sample was calcined *in situ* in an air flow by heating to 300 °C at a rate of 10 °C/min followed by a dwell of 30 min. The sample was outgassed until a residual pressure of  $5 \times 10^{-5}$  mbar was reached, followed by cooling to 50 °C in a static atmosphere of 2 mbar of O<sub>2</sub>. Then, CO pulses were added to the *in situ* cell in the presence of 2 mbar O<sub>2</sub>. CO was introduced via a sample loop with a volume of 10 μL. Pulses were administered to the cell until the IR bands related to adsorbed CO were saturated. For reduction, the sample was exposed to a H<sub>2</sub>/N<sub>2</sub> flow at 300 °C for 30 min after heating to this temperature at a rate of 5 °C/min. After reduction, the sample was evacuated and cooled to 50 °C. Then CO pulses were administered to the *in situ* cell as described above.

*In situ* EXAFS measurements were performed at the Pd K-edge using beam line 10ID-B of the Materials Research Collaborative Access Team at the Advanced Photon Source of Argonne National Laboratory (Lemont, USA). Typically, 50 mg of sample was mixed with 150 mg of inert silica powder in order to press pellets. The experiments were performed in a continuous flow reactor cell placed into a tube furnace. EXAFS data was recorded in fluorescence mode using a Pd foil as the reference. The experiments were performed on 2% wt Pd-loaded nanorods and 2% wt Pd-loaded nanocubes. The samples were studied in three conditions. The first “as-prepared” sample represents the state of the sample in air prior to treatment. Then, the sample was subjected to a 1 vol% CO/He flow (50 mL/min) at room temperature, followed by ramping to 200 °C at a rate of 2 °C/min in flowing CO. EXAFS spectra were collected after exposure to CO (spectra labelled “CO-treated”). Finally, the flow was switched to a 100 mL/min flow of 5 vol% O<sub>2</sub>/He and cooled to room temperature in order to follow the re-oxidation of the sample. Spectra were taken in O<sub>2</sub> at room temperature (spectra labelled “O<sub>2</sub>-treated”). Experimental EXAFS data  $\chi(k)$  (where  $k$  is the photoelectron wave number) were processed by subtracting the background from the normalized absorption coefficient using the Athena program of the IFEFFIT data analysis package [42]. The theoretical EXAFS signal was fitted to the data in *r*-space using the Artemis program of the IFEFFIT package.  $S_0^2$  (the passive electron reduction factor) was obtained by first analyzing a Pd foil, and then fixed at  $S_0^2 = 0.83$ . The *k*-range used for Fourier transform of  $\chi(k)$  was 2–10 Å<sup>-1</sup> and the *r*-range for fitting 1.0–2.2 Å for the as-prepared samples, 1.5–3.2 Å for CO-treated samples and 1.0–3.5 Å for O<sub>2</sub>-treated samples. Fits were performed simultaneously in *r*-space on  $k^1$ -,  $k^2$ -, and  $k^3$ -weighted spectra. The plotted spectra have a *k*-weight of 3. Selected parameters were shared in the fit:  $\sigma^2$  and *r* values were shared for Pd-O shells and for Pd-Pd shells.

### 2.3. Catalytic activity measurements

Catalytic activity measurements were performed in a 10-tube parallel microflow reactor. The samples were pressed, sieved and crushed and the fraction between 125 μm and 250 μm was used. Each quartz reactor was filled with 50 mg of sample diluted with 200 mg of SiC of the same sieve fraction. The mixture was enclosed between two quartz wool plugs. The reaction was performed at atmospheric pressure. Prior to reaction, the catalysts were calcined *in situ* in a flow consisting of 20 vol% O<sub>2</sub> in He (total flow rate 50 mL/min STP per reactor tube), whilst heating from room temperature to 300 °C at a rate of 5 °C/min, followed by an isothermal dwell of 3 h. After cooling to room temperature in the same flow, the pre-treatment gas was replaced by a feed consisting of 2 vol% CO and 2 vol% O<sub>2</sub> in He (total flow rate 50 mL/min STP). The temperature was increased by 25 °C steps at a rate of 5 °C/min. When the target temperature was reached, a period of 20 min was allowed for stabilization. Then, the effluent gas was analyzed by online gas chromatography with an Interscience Compact GC equipped with Plot (TCD) and Molsieve (TCD) columns.

### 2.4. Computational modeling

Density functional theory (DFT) with the PBE (Perdew-Burke-Ernzerhof) functional [43] as implemented in the Vienna Ab Initio Simulation (VASP) package [44,45] was used to simulate the CO oxidation by Pd-CeO<sub>2</sub>. A Hubbard *U* term was added to the PBE functional (DFT + *U*) employing the rotationally invariant formalism by Dudarev et al. [46], in which only the difference ( $U_{\text{eff}} = U - J$ ) between the Coulomb *U* and exchange *J* parameters enters. Spin-polarized calculations were performed. The projector augmented wave (PAW) method [47,48] was used to describe the interaction between the ions and the electrons with the frozen-core approximation. The Ce (4f, 5s, 5p, 5d, 6s), O (2s, 2p) and Pd (4p, 4d, 5s) electrons were treated as valence states using a plane-wave basis set with a kinetic energy cut-off of 400 eV. For Ce, a value of  $U_{\text{eff}} = 4.5$  eV was used, which was calculated self-consistency by Fabris et al. [49] using the linear response approach of Cococcioni and de Gironcoli [50]. This value is within 3.0–5.5 eV range reported to provide localization of the electrons in the Ce 4f orbital left upon oxygen removal from CeO<sub>2</sub> [51]. For all calculations, the model was a periodic slab with a (4 × 4) surface unit cell, and for the Brillouin zone integration, a Monkhorst-Pack 1 × 1 × 1 mesh was used. A higher *k*-point mesh only leads to a negligible energy differences. The CeO<sub>2</sub>(111) and CeO<sub>2</sub>(100) surface unit cells were both two layers thick, and the vacuum gap was set to 15 Å. The bulk equilibrium lattice constant (5.49 Å) previously calculated by PBE + *U* ( $U_{\text{eff}} = 4.5$  eV) was used [52]. The CeO<sub>2</sub>(111) surface exposes three-fold coordinated O atoms as well as seven-fold coordinated Ce atoms, and the CeO<sub>2</sub>(100) surface exposes two-fold coordinated O and six-fold coordinated Ce atoms. It is noted that the CeO<sub>2</sub>(111) surface has a compact structure consisting of an uninterrupted Ce-O bond network, whereas the CeO<sub>2</sub>(100) surface contains separated rows of CeO<sub>2</sub> units. The bottom layer was fixed to the bulk position of CeO<sub>2</sub>, while the top layer was allowed to relax. The positions of the atoms were relaxed until forces were smaller than 0.05 eV Å<sup>-1</sup>. For investigating the reaction mechanism, the location and energy of stable and transition states were calculated with the climbing-image nudged elastic band (CI-NEB) method [53].

We computed the IR intensity of stretching vibrational modes of adsorbed CO to support the interpretation of CO IR spectra. For this purpose, a finite difference analysis was employed to stable CO adsorption structures. The first-order IR intensity of the *i*th mode is given by Porezag et al. [53,54].

$$I_i^{IR} \propto \left| \frac{d\mu}{dQ_i} \right|^2 \quad (1)$$

where  $Q_i$  is referred to as a normal mode coordinate and  $\mu$  is the electric dipole moment of the system.

Microkinetics simulations were performed to compute reaction rates based on a reaction mechanism for CO oxidation for which the potential energy surface was determined by DFT calculations. The approach to microkinetics simulations has been presented in detail elsewhere [55,56]. Differential equations for all the surface reaction intermediates were constructed using the rate constants and the set of elementary reaction steps. For each of the  $M$  components in the kinetic network, a single differential equation is obtained in the form as below:

$$r_i = \sum_{j=1}^N \left( k_j \nu_i^j \prod_{k=1}^M c_k^{\nu_k^j} \right) \quad (2)$$

In this equation,  $k_j$  is the elementary reaction rate constant (see Eq. 5),  $\nu_i^j$  is the stoichiometric coefficient of component  $i$  in elementary reaction step  $j$  and  $c_k$  is the concentration of component  $k$  on the catalytic surface.

For surface reactions, the rate constants of the forward and backward elementary reaction were determined by the Eyring equation [57]:

$$k = \frac{k_b T}{h} \frac{Q^{TS}}{Q} e^{-\frac{E_a}{k_b T}} \quad (3)$$

where  $k$  is the reaction rate constant in  $s^{-1}$ ;  $k_b$ ,  $T$ ,  $h$  and  $E_a$  are the Boltzmann constant, temperature, Planck's constant and the activation barrier, respectively.  $Q^{TS}$  and  $Q$  refer the partition functions of the transition and ground states, respectively. As an approximation, the pre-factor is set to  $10^{13} s^{-1}$  for all the elementary surface reactions.

For non-activated molecular adsorption, the rate of adsorption is determined by the rate of surface impingement of gas-phase molecules. The flux of incident molecules is given by Hertz-Knudsen equation [58]:

$$F = \frac{P}{\sqrt{2\pi m k_b T}} \quad (4)$$

Therefore, the molecular adsorption rate constant can be written as:

$$k_{ads} = \frac{PA'}{\sqrt{2\pi m k_b T}} S \quad (5)$$

where  $P$  is the partial pressure of the adsorbate in the gas phase,  $A'$  is the surface area of the adsorption site,  $m$  is the mass of the adsorbate, and  $S$  is the sticking coefficient.

For the desorption process, it is assumed that there are three rotational degrees of freedom and two translational degrees of freedom in the transition state. Accordingly, the rate of desorption is given by

$$k_{des} = \frac{k_b T^3}{h^3} \frac{A'(2\pi k_b)}{\sigma \theta_{rot}} e^{-\frac{E_{des}}{k_b T}} \quad (6)$$

where  $\sigma$  and  $\theta$  are the symmetry number and the characteristic temperature for rotation of gaseous  $CO_2$ , respectively.  $E_{des}$  is the desorption energy of  $CO_2$  molecules.

Microkinetics simulations were performed using the MKMCXX program [55,56,59]. Steady-state coverages were calculated by integrating ordinary differential equations (ODEs) that describe the changes in surface coverages with time until the changes in the surface coverages were very small. As chemical systems typically give rise to stiff sets of ODEs, we have used the backward differentiation formula method for the time integration [56]. The rates of the individual elementary reaction steps can be obtained based on the steady-state surface coverages. Our simulations were carried out using a gaseous feed mixture of CO and  $O_2$  in 2:1 M ratio at a total pressure of 1 atm and a temperature of 50 °C.

The elementary reaction steps that contribute to the rate control over the overall reaction can be determined by degree of rate control (DRC) concept introduced by Campbell et al. [60–62]. For elementary step  $i$ , the degree of rate control  $X_{RC,i}$  can be defined as

**Table 1**

Summary of the properties of the  $CeO_2$ -rod and  $CeO_2$ -cube supports and the Pd-loaded catalysts derived thereof.

Catalyst	BET surface area ( $m^2/g$ )	Particle size (nm) $CeO_2$ by TEM	XRD linewidth of the (111) peak (degrees)	ICP-OES Pd loading (%)
Pd/ $CeO_2$ -rod	78	11 ± 2 (width) 160 ± 50 (length)	0.57	1.33 ± 0.02
Pd/ $CeO_2$ -cube	28	17 ± 4	0.22	1.37 ± 0.02

$$X_{RC,i} = \frac{k_i}{r} \left( \frac{\partial r}{\partial k_i} \right)_{k_j \neq i, K_i} = \left( \frac{\partial \ln r}{\partial \ln k_i} \right)_{k_j \neq i, K_i} \quad (7)$$

where  $k_i$ ,  $K_i$  and  $r$  are the rate constants, the equilibrium constant for step  $i$  and the reaction rate, respectively. Furthermore, the DRC coefficients have to obey the sum rule over all steps  $i$  in the mechanism in such a way that [61]:

$$\sum_i X_{RC,i} = 1 \quad (8)$$

### 3. Results and discussion

$CeO_2$  nanorods and nanocubes were prepared by a modified hydrothermal synthesis method in which a basic aqueous cerium nitrate solution was treated in an autoclave under autogenous water pressure at, respectively, 100 °C and 180 °C. XRD patterns confirm that the calcined supports have the cubic fluorite structure ( $Fm\bar{3}m$  space group) of  $CeO_2$  (not shown). The specific surface areas as determined by  $N_2$  physisorption are 78  $m^2/g$  and 28  $m^2/g$  for the ceria nanorods and nanocubes, respectively (Table 1). A high-resolution SEM (HR-SEM) analysis confirms the morphology of the two samples (Fig. 1). This analysis also shows that the nanorods also contain some very small  $CeO_2$  particles of poorly defined shape at their surface.

From aberration-corrected TEM (AC-TEM) images (Fig. 2), we determined that the  $CeO_2$ -rod sample contains nanorods with an average width of 11 ± 2 nm and an average length of 160 ± 50 nm, as reported in Table 1. The average size of the nanocubes is 17 ± 4 nm. In line with the HR-SEM images, both samples present a small fraction of  $CeO_2$  polyhedra. The  $CeO_2$ -rod sample exposes predominantly the (111) surface with a large amount of corrugations and surface defects, in line with earlier reports [17,41,63]. Conversely, the  $CeO_2$ -cubes selectively expose prominent (001) surfaces (Fig. 2b). Additionally, the surface appears to be irregular due to its polarity. The (110) surface is not stable and forms (111) microfacets. Due to the tilting along the [110] zone axis, the (110) is visualized at its thinnest point, allowing the atomic rows to be clearly resolved. Pd was loaded on these supports by a conventional incipient wetness impregnation procedure. The presence of ~1 wt% Pd on Pd/ $CeO_2$ -rod and Pd/ $CeO_2$ -cube was confirmed by elemental analysis. In the TEM images, the surface of the nanorods does not exhibit any Pd nanoparticles, which is consistent with earlier work [41] and indicative of a very high Pd dispersion (Fig. 2c). On the other hand, in Fig. 2d distinct Pd nanoparticles can be seen in the Pd/ $CeO_2$ -cube sample [17]. The average size of these Pd particles is ~2 nm.

We determined the catalytic performance of the bare  $CeO_2$  supports and the ceria-supported Pd catalysts in the CO oxidation reaction. Prior to reaction, the samples were calcined at 300 °C. The CO conversion with increasing temperature is shown in Fig. 3. As expected, the  $CeO_2$  supports themselves are only active at high temperature. The Pd/ $CeO_2$ -rod sample displays a higher activity than the Pd/ $CeO_2$ -cube one. Pd/ $CeO_2$ -rod already shows activity at room temperature and achieves full CO conversion below 150 °C [41]. Full CO conversion is achieved by the

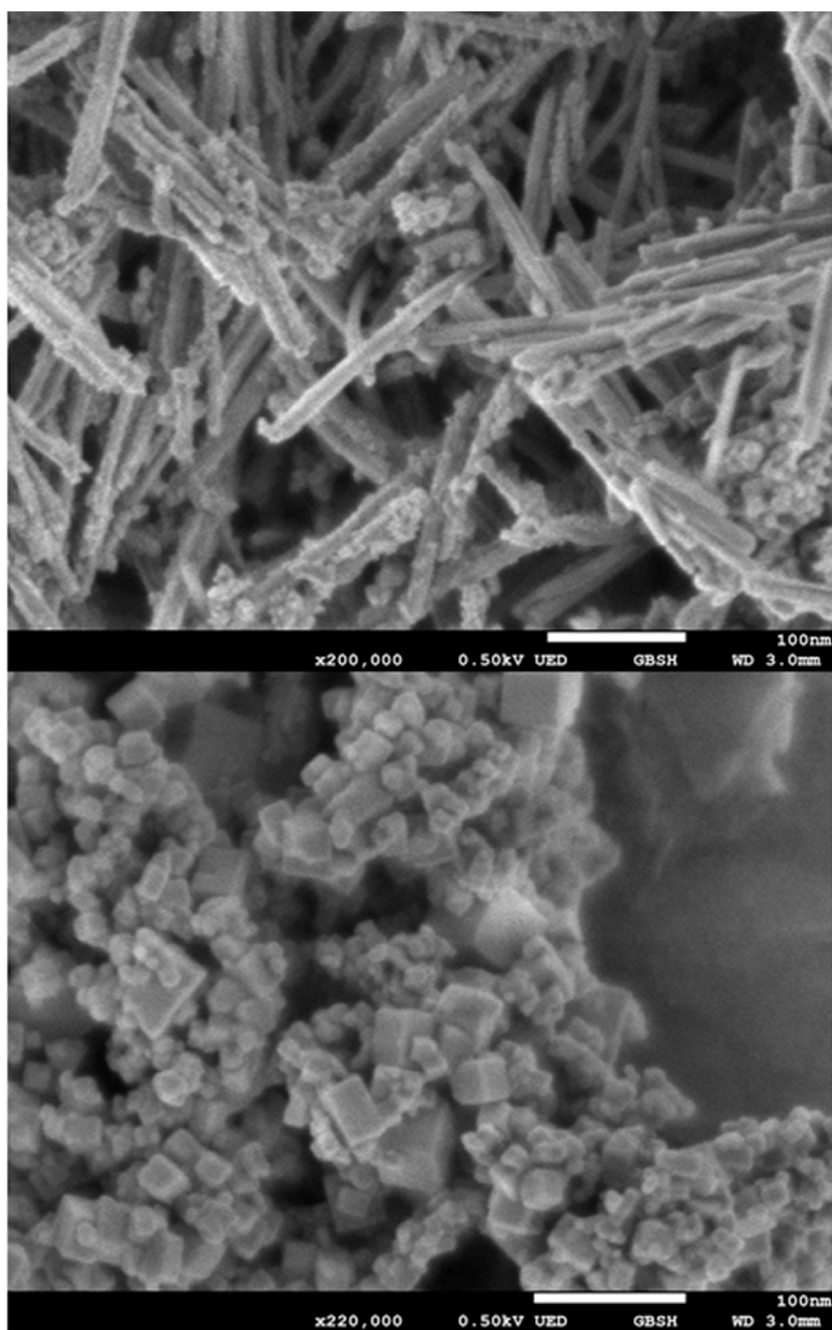


Fig. 1. HR-SEM images of  $\text{CeO}_2$ -rods (top) and  $\text{CeO}_2$ -cubes (bottom).

$\text{Pd}/\text{CeO}_2$ -cube sample only at 200 °C. Additionally, the evaluation of the CO oxidation activity, while cooling down as well as in a heating step demonstrated the stability of these catalysts, as reported in the Supporting Information. The higher CO oxidation activity for the nanorod sample is also in line with other reports [18,40,64]. A reference 5 wt%  $\text{Pd}/\text{SiO}_2$  sample was also evaluated in the same reaction. TEM analysis showed the presence of ~3 nm Pd nanoparticles. This sample displayed much lower activity than the two  $\text{Pd}/\text{CeO}_2$  samples, indicating that there is a  $\text{Pd}-\text{CeO}_2$  synergy in CO oxidation for both  $\text{Pd}/\text{CeO}_2$ -rod and  $\text{Pd}/\text{CeO}_2$ -cube. In order to further compare the activity of these samples, CO conversion rates were calculated normalized by the palladium weight. At 50 °C,  $\text{Pd}/\text{CeO}_2$ -rod displays a rate of  $1 \times 10^{21}$  molecules  $\text{CO g}_{\text{Pd}}^{-1} \text{s}^{-1}$ , while  $\text{Pd}/\text{CeO}_2$ -cube and  $\text{Pd}/\text{SiO}_2$  presented lower values of  $3 \times 10^{20}$  and  $2 \times 10^{20}$  molecules  $\text{CO g}_{\text{Pd}}^{-1} \text{s}^{-1}$ , respectively. These differences were even more pronounced at a temperature

of 100 °C, with  $\text{Pd}/\text{CeO}_2$ -rod and  $\text{Pd}/\text{CeO}_2$ -cubes reaching rates of  $9 \times 10^{21}$  and  $1 \times 10^{21}$  molecules  $\text{CO g}_{\text{Pd}}^{-1} \text{s}^{-1}$ , respectively, while the reaction rate of  $\text{Pd}/\text{SiO}_2$  only was  $2 \times 10^{19}$  molecules  $\text{CO g}_{\text{Pd}}^{-1} \text{s}^{-1}$ .

As discussed before, the absence of Pd particles on  $\text{CeO}_2$ -rods is indicative of a very high Pd dispersion, which can explain the high catalytic activity [41]. Conversely, the presence of Pd nanoparticles on the surface of the  $\text{Pd}/\text{CeO}_2$ -cube sample can in principle provide a reasonable explanation for the much lower activity of this sample. We considered that  $\text{Pd}/\text{CeO}_2$ -cube might also contain highly dispersed Pd in addition to the TEM-visible nanoparticles. Therefore, we decided to investigate this sample in much more detail using the methods previously used to investigate the presence of isolated Pd atoms in  $\text{Pd}/\text{CeO}_2$ -rod [41].

Fig. 4 shows *in situ* CO IR spectra of  $\text{Pd}/\text{CeO}_2$ -rod and  $\text{Pd}/\text{CeO}_2$ -cube samples at 50 °C. Before CO dosing, the samples were first calcined at

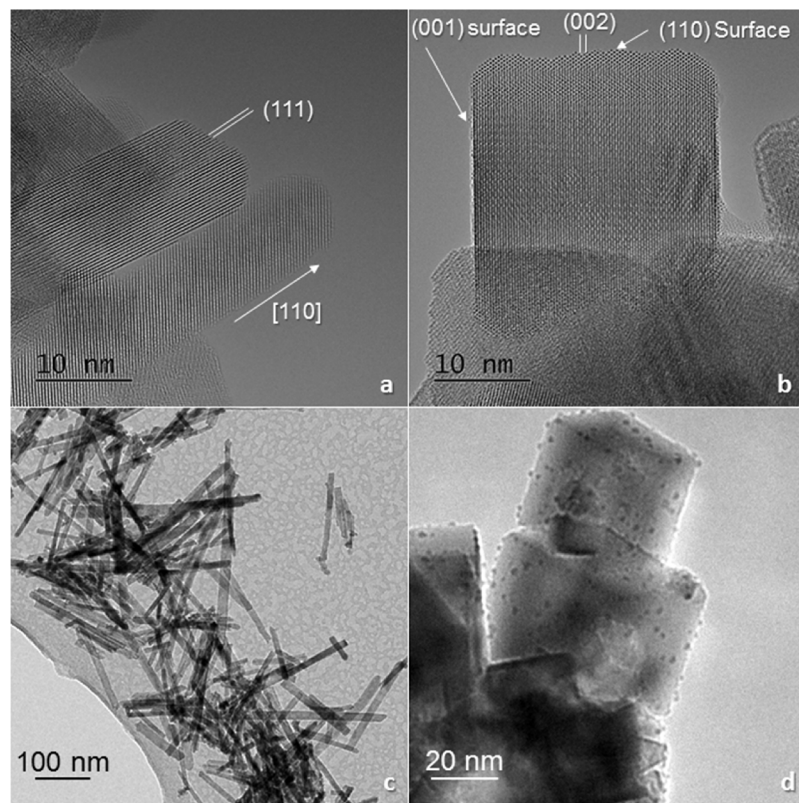


**Fig. 2.** AC-TEM images of (a) CeO<sub>2</sub>-rods, and (b) CeO<sub>2</sub>-cubes with indication of the most prominent planes, and TEM images of (c) Pd/CeO<sub>2</sub>-rods and (d)) Pd/CeO<sub>2</sub>-cube.

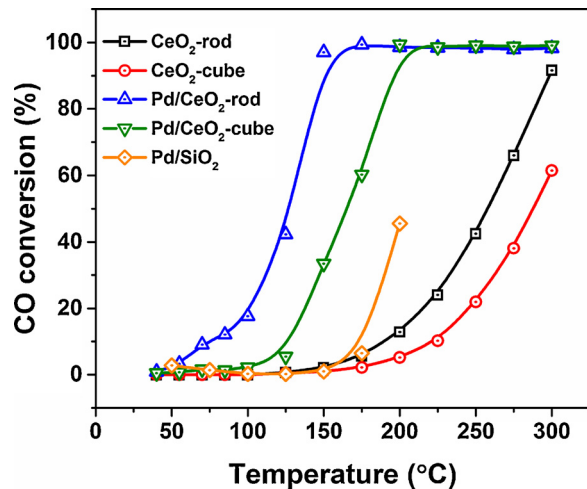


**Fig. 3.** CO conversion in the CO oxidation reaction on pre-oxidized CeO<sub>2</sub>-rod, CeO<sub>2</sub>-cube, Pd/CeO<sub>2</sub>-rod, Pd/CeO<sub>2</sub>-cube and Pd/SiO<sub>2</sub> catalysts.

300 °C and cooled to 50 °C in the presence of 2 mbar O<sub>2</sub>. We did not evacuate the samples before CO pulsing. The bands developing around 2352 cm<sup>-1</sup> are due to gaseous CO<sub>2</sub> and indicate that CO oxidation takes place at this low temperature. The much higher intensity of the CO<sub>2</sub> IR bands for Pd/CeO<sub>2</sub>-rod compared to Pd/CeO<sub>2</sub>-cube is in qualitative agreement with the activity difference in Fig. 3. For Pd/CeO<sub>2</sub>-rod, the band at 2143 cm<sup>-1</sup> was earlier assigned to a Pd<sub>1</sub>O<sub>2</sub> species, while the peak at 2098 cm<sup>-1</sup> was attributed to a Pd<sub>1</sub>O species. These assignments were supported by DFT calculations of Pd<sub>1</sub>O<sub>x</sub>/CeO<sub>2</sub>(111) models. The broad band with a lower intensity around 1900 cm<sup>-1</sup> was attributed to small partially-oxidized Pd clusters, as the IR band could be correlated using DFT to CO adsorbed on a ceria-supported Pd<sub>3</sub>O cluster [41]. The

presence of CO IR bands for Pd<sub>1</sub>O and Pd<sub>1</sub>O<sub>2</sub> sites is consistent with their role as major reaction intermediates in the catalytic CO oxidation cycle [41].

The CO IR spectra for Pd/CeO<sub>2</sub>-cube are different. The most intense band is located at 2098 cm<sup>-1</sup>. The presence of this band is a strong indication for the presence of isolated Pd species on the cube surface as well. The low intensity of the band at 2146 cm<sup>-1</sup> shows that a more oxidized form of a single Pd atom is present only in small quantities.

In order to assess the possible role of isolated Pd species on the CeO<sub>2</sub>(100) surface in CO oxidation, we performed a detailed DFT study, as previously done for Pd/CeO<sub>2</sub>-rod [41]. DFT calculations in combination with a thermodynamic analysis can help to identify thermodynamically stable structures, which are candidates for catalysis [65]. For a single Pd atom on the CeO<sub>2</sub>(100) surface, we determined the stability of Pd<sub>1</sub>O<sub>x</sub> structures with  $x = 0\text{--}3$ , which are depicted in Fig. 5a. A Helmholtz free energy analysis [66] of these structures shows that under typical reaction conditions Pd<sub>1</sub>O/CeO<sub>2</sub> should be considered to be part of a catalytic CO oxidation cycle (Fig. 5b).

CO adsorption on these Pd<sub>1</sub>O<sub>x</sub>/CeO<sub>2</sub>(100) models was also investigated (Fig. 5c). Adsorption energies and further details for Pd<sub>1</sub>O<sub>x</sub>/CeO<sub>2</sub>(100) and Pd<sub>1</sub>O<sub>x</sub>/CeO<sub>2</sub>(111) are listed in Table 2. The computed value for Pd<sub>1</sub>O/CeO<sub>2</sub>(100) of 2099 cm<sup>-1</sup> is very close to the experimental value of the most intense peak (2098 cm<sup>-1</sup>) in the CO IR spectrum. Different from CeO<sub>2</sub>(111), a Pd<sub>1</sub>O<sub>2</sub> species located on the (100) surface does not adsorb CO. CO adsorption on a single Pd atom on CeO<sub>2</sub>(100) results in an adsorption band at 2071 cm<sup>-1</sup>, which is experimentally observed as a weak shoulder in the CO IR spectra of Pd/CeO<sub>2</sub>-cube. We speculate that the weak band at 2141 cm<sup>-1</sup> is due to a small amount Pd<sub>1</sub>O<sub>2</sub> species on CeO<sub>2</sub>(111) or a dicarbonyl Pd(CO)<sub>2</sub> species adsorbed on Pd/CeO<sub>2</sub>(100). The relatively late appearance of this band is in line with the computed weaker CO adsorption of the dicarbonyl species. Notably, the other vibrational mode of the dicarbonyl, which should appear at 2112 cm<sup>-1</sup>, is not observed because

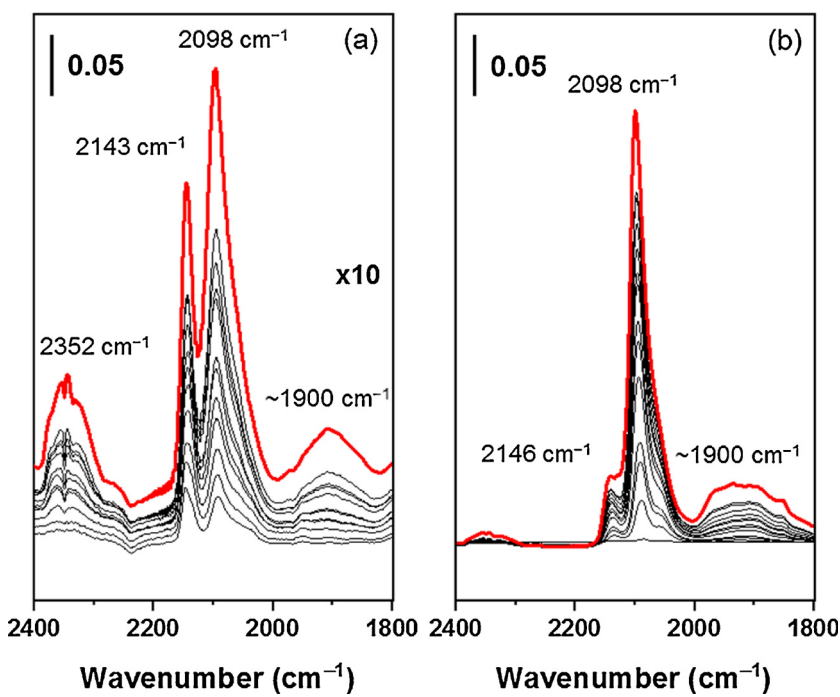
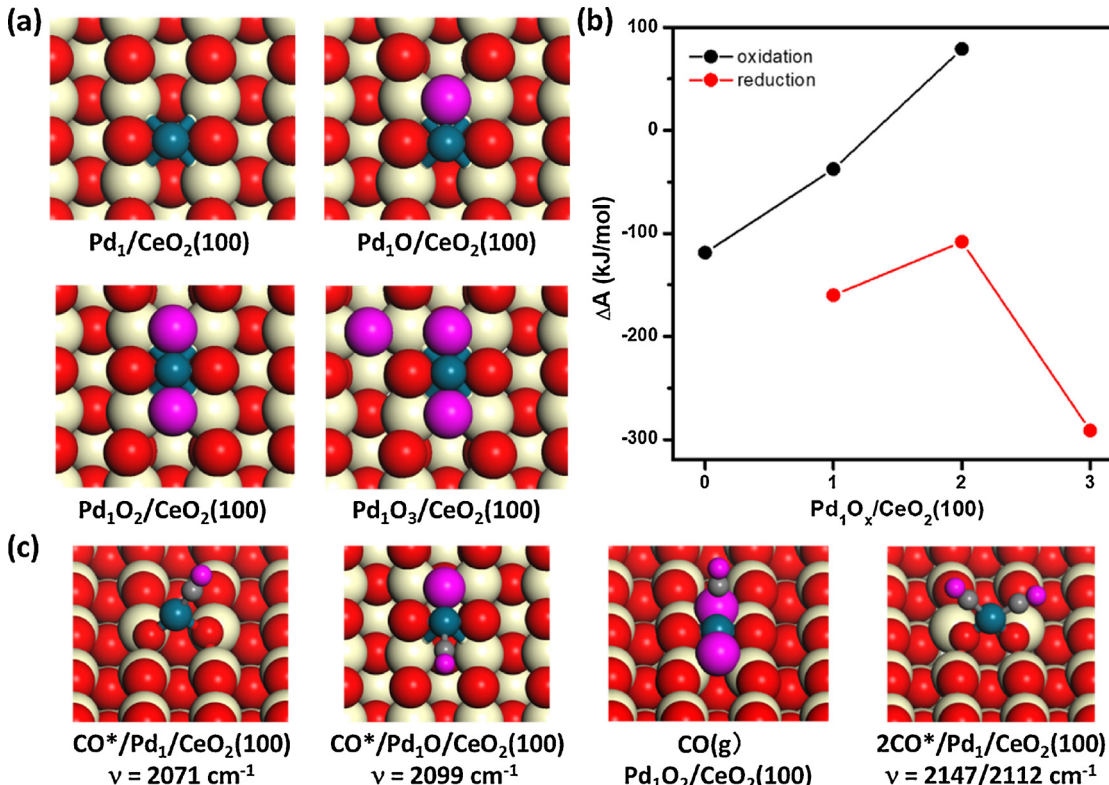


**Fig. 4.** CO IR spectra of (a) Pd/CeO<sub>2</sub>-rod and (b) Pd/CeO<sub>2</sub>-cube recorded at 50 °C. The spectra represent subsequent pulses of CO added to an atmosphere of 2 mbar of O<sub>2</sub>. The pulses were protracted until a quantity of 2 mbar of CO was reached (red spectra) (For interpretation of the references to colour in this figure legend, the reader is referred to the web version of this article).

of a very low IR intensity (Table 2).

The CO IR data combined with the DFT calculations strongly suggests that the Pd/CeO<sub>2</sub>-cube sample also contains isolated Pd atoms, predominantly in the form of Pd<sub>1</sub>O. Compared to similar species involved in CO oxidation on CeO<sub>2</sub>(111), their activity is apparently much lower. To understand this in more detail, we carried out a study of the

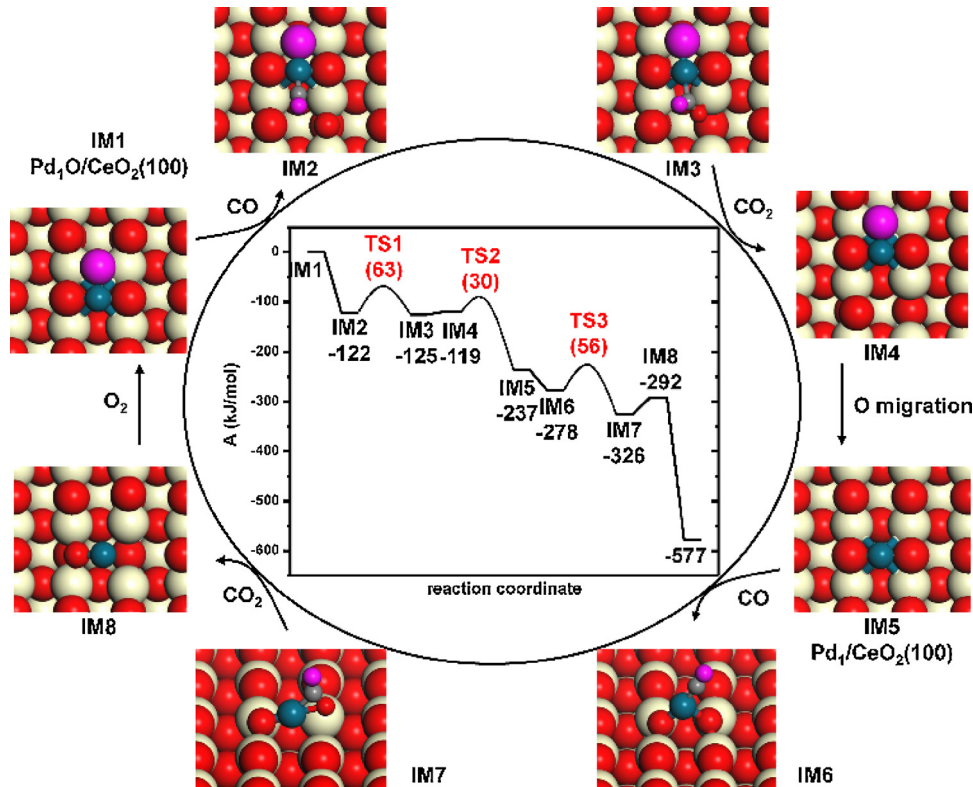
mechanism of CO oxidation on Pd<sub>1</sub>/CeO<sub>2</sub>(100). The resulting Helmholtz free energy diagram is shown in Fig. 6b. CO adsorbs with an energy of 122 kJ/mol on Pd<sub>1</sub>O/CeO<sub>2</sub>(100). This value includes an entropy correction for gaseous CO. CO<sub>2</sub> formation preferentially occurs via reaction of adsorbed CO with a ceria lattice O atom (IM2 → IM3). The barrier for this process is 63 kJ/mol (TS1). The resulting CO<sub>2</sub>



**Fig. 5.** (a) DFT-optimized structures of Pd<sub>1</sub>, Pd<sub>1</sub>O and Pd<sub>1</sub>O<sub>2</sub> sites on the CeO<sub>2</sub>(100) surface (color scheme: red, surface O; white, surface Ce; pink, O of adsorbed species; blue, Pd); (b) Helmholtz free energy analysis of the stability of Pd<sub>1</sub>O<sub>x</sub>/CeO<sub>2</sub>(100) during reduction by CO and oxidation by O<sub>2</sub>. Each point represents an oxidation or reduction reaction of Pd<sub>1</sub>O<sub>x</sub> by ½ O<sub>2</sub> or CO, respectively; (c) Structures and predicted frequencies of CO adsorbed on Pd<sub>1</sub>O<sub>x</sub>/CeO<sub>2</sub>(100) models. (For interpretation of the references to colour in this figure legend, the reader is referred to the web version of this article).

**Table 2**DFT-computed adsorption energies for CO on  $\text{Pd}_x\text{O}_y/\text{CeO}_2(111)$  and  $\text{Pd}_x\text{O}_y/\text{CeO}_2(100)$ , and related IR frequencies and intensities.

Species	$\text{CeO}_2(111)$			$\text{CeO}_2(100)$		
	$\text{CO}/\text{Pd}_1\text{O}_2$	$\text{CO}/\text{Pd}_1\text{O}$	$\text{CO}/\text{Pd}_1$	$2\text{CO}/\text{Pd}_1$	$\text{CO}/\text{Pd}_1\text{O}$	$\text{CO}/\text{Pd}_1$
$E_{\text{ads}}$ (kJ/mol)	−117	−154	−216	−100/−137	−181	−100
Frequency ( $\text{cm}^{-1}$ )	2137	2098	2048	2147/2112	2099	2071
Intensity (a.u.)	0.54	0.45	0.52	0.39/0.005	0.28	0.73

**Fig. 6.** Helmholtz free energy analysis of CO oxidation on a  $\text{Pd}_1\text{O}/\text{CeO}_2(100)$  surface model (energies are shown for  $T = 50^\circ\text{C}$ ).

molecule is weakly bound. By including the entropy correction, we find that desorption only costs 6 kJ/mol ( $\text{IM}3 \rightarrow \text{IM}4$ , Fig. 6). The reaction of adsorbed CO by the non-lattice oxygen atom in  $\text{Pd}_1\text{O}/\text{CeO}_2(100)$  is geometrically hindered. Once  $\text{CO}_2$  desorbs, the O atom coordinated to the Pd site will migrate via a transition state with a barrier of only 30 kJ/mol (TS2, Fig. 6) to the oxygen vacancy in the ceria support. The resulting structure is  $\text{Pd}_1/\text{CeO}_2(100)$  (IM5). A second CO molecule can then adsorb on the surface with a Helmholtz free energy of adsorption of 39 kJ/mol.  $\text{CO}_2$  is formed in a similar manner ( $\text{IM}6 \rightarrow \text{IM}7$ ) via transition state TS3 with an activation barrier of 56 kJ/mol. Desorption of  $\text{CO}_2$  is again facile and the catalytic cycle closes by adsorption and spontaneous dissociation of molecular  $\text{O}_2$ , regenerating  $\text{Pd}_1/\text{CeO}_2(100)$ .

It is important to point out that the mechanism for low-temperature CO oxidation is different for  $\text{Pd}/\text{CeO}_2(111)$  and  $\text{Pd}/\text{CeO}_2(100)$ . For  $\text{Pd}/\text{CeO}_2(111)$ , only non-lattice O atoms of  $\text{PdO}$  and  $\text{PdO}_2$  species are involved in the catalytic cycle [41]. This resembles a Langmuir-Hinshelwood mechanism in which CO and  $\text{O}_2$  adsorb on the catalytic surface. In contrast, CO oxidation on  $\text{Pd}/\text{CeO}_2(100)$  involves a ceria lattice O atom and thus follows a Mars-van Krevelen mechanism. This difference is caused by two effects. The first one is the high barrier for the reaction between adsorbed CO and the non-lattice O atom in  $\text{Pd}_1\text{O}/\text{CeO}_2(100)$ , which stems from an unfavorable geometry. The second is the lower oxygen vacancy formation energy of the  $\text{CeO}_2(100)$  surface as compared to  $\text{CeO}_2(111)$ . The DFT-computed O vacancy formation energies

for these surfaces are 1.80 eV and 2.38 eV, respectively. Experiments have confirmed that it is easier to form O vacancies on the (100) surface than on the (111) surface [67]. Furthermore, the free activation barriers for CO oxidation in a catalytic cycle involving  $\text{Pd}_1\text{O}$  and  $\text{Pd}_1\text{O}_2$  on  $\text{CeO}_2(111)$  are much lower (29 kJ/mol) compared to the values for  $\text{Pd}_1$  and  $\text{Pd}_1\text{O}$  on  $\text{CeO}_2(100)$  (highest barrier 63 kJ/mol). In essence, the geometry of the  $\text{Pd}_1\text{O}$  species on  $\text{CeO}_2(100)$  does not allow for CO oxidation with the non-lattice O atom and, therefore, the reaction occurs via a Mars-van Krevelen mechanism. The geometrical aspect is emphasized by noting that the Pd-O binding energy of  $\text{Pd}_1\text{O}$  on  $\text{CeO}_2(100)$  is lower than the O vacancy formation energy for  $\text{CeO}_2(100)$ . This energy difference also explains why migration of the non-lattice O atom to the O vacancy is exothermic. We carried out microkinetics simulations for the catalytic cycles of  $\text{Pd}/\text{CeO}_2(100)$  and  $\text{Pd}/\text{CeO}_2(111)$  at a temperature of 50 °C. Given that we did not compute all the partition functions in great detail, the predicted rates are order of magnitude estimates largely determined by the differences in the overall activation barriers in the mechanisms. The estimated rate for  $\text{Pd}/\text{CeO}_2(100)$  is substantially lower than that for  $\text{Pd}/\text{CeO}_2(111)$ , providing a reasonable explanation for the experimentally observed activity difference.

We also recorded CO IR spectra after *in situ* reduction in  $\text{H}_2$  at 300 °C. After cooling to 50 °C, the spectra were obtained as a function for the CO coverage (in the absence of  $\text{O}_2$ ). Fig. 7 shows the resulting spectra after saturation of the bands for  $\text{Pd}/\text{CeO}_2$ -cube and  $\text{Pd}/\text{CeO}_2$ -

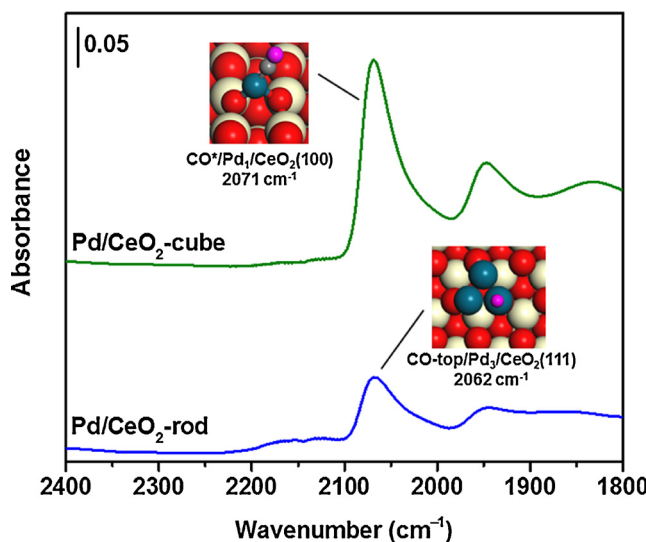


**Fig. 7.** CO IR spectra of reduced Pd/CeO<sub>2</sub>-rod (blue) and Pd/CeO<sub>2</sub>-cube (green) exposed to 2 mbar of CO at 50 °C. The catalysts were previously reduced *in situ* at 300 °C in H<sub>2</sub> and then evacuated while cooling to 50 °C. The inserts show DFT-optimized structures of CO on different Pd configurations on CeO<sub>2</sub>(111) and CeO<sub>2</sub>(100) (For interpretation of the references to colour in this figure legend, the reader is referred to the web version of this article).

rod. After reduction, the spectra of the two samples look qualitatively similar but very different from IR spectra obtained under CO oxidation conditions. The weak bands in the 2200–2100 cm<sup>-1</sup> can be attributed to electronic transitions of Ce<sup>3+</sup>, which was formed in large quantities during reduction [68]. The main IR bands between 2100 cm<sup>-1</sup> and 2000 cm<sup>-1</sup> observed in the spectra are due to CO adsorption on small reduced Pd clusters in high dispersion [69]. The CO IR bands in Fig. 7 might be mainly caused by highly dispersed Pd clusters originating from reduction of the predominantly isolated PdO<sub>x</sub> species. From this, we conclude that the Pd nanoparticles observed by TEM constitute a relatively small fraction of Pd present in the sample.

In order to better understand the dynamics of the two catalysts, we carried out an *in situ* EXAFS study in which the Pd phase in Pd/CeO<sub>2</sub>-rod and Pd/CeO<sub>2</sub>-cube samples was followed in different gas atmospheres. The Pd loading for these samples was 2% wt. The as-prepared (non-calcined) samples contains Pd-oxide as evident from Pd-O and Pd-Pd first and second coordination shells (Fig. 8) [31,70]. When treated in CO at 200 °C, the Pd-oxide phase is reduced, which is evident from the loss of the Pd-O shell and the appearance of a clear Pd-Pd metal shell (Table 3). When the samples are re-oxidized again at 200 °C in O<sub>2</sub>, the

Pd/CeO<sub>2</sub>-rod sample re-oxidizes more easily (the oxidation degree is about 60% based on the Pd-O coordination number, *i.e.*, the fully oxidized PdO has 4 Pd-O bonds) compared to an oxidation degree of approximately 30% for Pd/CeO<sub>2</sub>-cube. The partial re-oxidation of the Pd/CeO<sub>2</sub>-rod sample is also evident by the reappearance of the Pd-O shell (Fig. 8). These results suggest that upon re-oxidation, the Pd in the Pd/CeO<sub>2</sub>-rod sample is able to partially redisperse into smaller clusters over the support, while the Pd in the Pd/CeO<sub>2</sub>-cube sample remains in the aggregated reduced state.

#### 4. Conclusions

We investigated in detail the surface of a 1 wt% Pd catalyst supported on nanocubes of CeO<sub>2</sub>, whose surface is predominantly enclosed by (100) facets. The resulting data are compared to our earlier findings for Pd supported on nanorods of CeO<sub>2</sub> supported on ceria (111) surfaces. Pd/CeO<sub>2</sub>-cube is much less active than Pd/CeO<sub>2</sub>-rod, but more active than Pd/SiO<sub>2</sub>. This shows that there is synergy between the Pd phase and the CeO<sub>2</sub>(100), although its extent is less than the Pd-CeO<sub>2</sub>(111) synergy. HR-TEM shows that the surface of Pd/CeO<sub>2</sub>-cube contains nanoparticles. CO IR spectroscopy evidences that the surface also contains highly dispersed Pd species, similar to Pd/CeO<sub>2</sub>-rod. DFT calculations suggest that Pd<sub>1</sub>O is a predominant species during CO oxidation, while also small amounts of Pd<sub>1</sub>O<sub>2</sub> and Pd<sub>1</sub> are observed by IR spectroscopy. Using DFT, we also constructed a catalytic cycle. Due to an unfavorable geometry, CO adsorbed to Pd<sub>1</sub>O on CeO<sub>2</sub>(100) will not react with the non-lattice O atom. Instead, CO reacts with a ceria lattice O atom. This Mars-van Krevelen pathway is possible because the lattice O atom in CeO<sub>2</sub>(100) is less strongly bonded than the lattice O atom in CeO<sub>2</sub>(111). Due to the relatively weak Pd-O bond strength, the non-lattice O atom migrates to the surface O vacancy. Further CO adsorption on reduced Pd results in another Mars-van Krevelen event. The resulting Pd atom close to a ceria O vacancy transforms in Pd<sub>1</sub>O on the stoichiometric surface by O<sub>2</sub> adsorption and dissociation. This catalytic cycle is less favorable than the one involving Pd<sub>1</sub>O and Pd<sub>1</sub>O<sub>2</sub> on CeO<sub>2</sub>(111) in which a Langmuir-Hinshelwood mechanism is followed. The difference in free energy barriers explains well why Pd/CeO<sub>2</sub>-rods are active at room temperature, while Pd/CeO<sub>2</sub>-cubes can only oxidize CO at higher temperature. Finally, EXAFS measurements show that the active Pd phase in both Pd/CeO<sub>2</sub>-rods and Pd/CeO<sub>2</sub>-cubes responds dynamically with respect to reducing and oxidizing conditions. The redispersion of Pd in oxidative conditions is more pronounced for Pd/CeO<sub>2</sub>-rods.

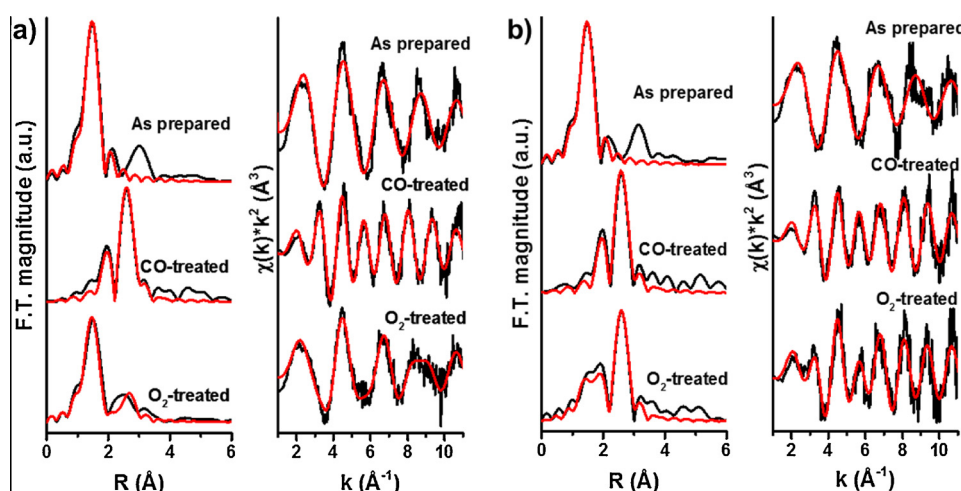


**Fig. 8.** Fourier-transformed and k space Pd K-edge EXAFS spectra of (a) Pd/CeO<sub>2</sub>-rod and (b) Pd/CeO<sub>2</sub>-cube in as-prepared (top), CO-treated (middle) and O<sub>2</sub>-treated states (bottom). The black curves represent the data, while the red curves represent the fittings (For interpretation of the references to colour in this figure legend, the reader is referred to the web version of this article).

**Table 3**Pd K-edge EXAFS fitting results for the Pd/CeO<sub>2</sub>-rod and Pd/CeO<sub>2</sub>-cube sample.

Pd/CeO <sub>2</sub> -rod					Pd/CeO <sub>2</sub> -cube				
Conditions	Shell	N	R (Å)	$\sigma^2$ (*10 <sup>3</sup> ) (Å <sup>2</sup> )	Conditions	Shell	N	R (Å)	$\sigma^2$ (*10 <sup>3</sup> ) (Å <sup>2</sup> )
As prepared	Pd-O	3.9 ± 0.2	1.99 ± 0.010	1.8	As prepared	Pd-O	3.8 ± 0.4	2.00 ± 0.010	1.6
CO-treated	Pd-Pd	8.9 ± 0.9	2.74 ± 0.010	12	CO-treated	Pd-Pd	8.5 ± 0.8	2.73 ± 0.010	9.8
O <sub>2</sub> -treated	Pd-O	2.6 ± 0.3	1.99 ± 0.010	1.8	O <sub>2</sub> -treated	Pd-O	1.1 ± 0.3	2.00 ± 0.010	1.6
	Pd-Pd	2.4 ± 0.7	2.74 ± 0.010	12		Pd-Pd	7.9 ± 1	2.73 ± 0.010	9.8

**Acknowledgments**

E.J.M.H. thanks the Netherlands Organization for Scientific Research (NWO) for a personal Vici research grant (number 13708). AKD acknowledges support from the U.S. Department of Energy, Office of Science through grant DE-FG02-05ER15712 for the research performed at UNM. The EXAFS measurements were carried out at the Advanced Photon Source using the MRCAT beam lines. Use of the Advanced Photon Source was supported by the U.S. Department of Energy, Office of Basic Energy Sciences, under contract No. DE-AC02-06CH11357. MRCAT operations are supported by the Department of Energy and the MRCAT member institutions. The authors would like to thank Dr. Lennart van Haandel for his help with the EXAFS data analysis.

**Appendix A. Supplementary data**

Supplementary material related to this article can be found, in the online version, at doi:<https://doi.org/10.1016/j.apcatb.2018.10.015>.

**References**

- [1] N. Izu, W. Shin, N. Murayama, S. Kanzaki, Resistive oxygen gas sensors based on CeO<sub>2</sub> fine powder prepared using mist pyrolysis, *Sens. Actuators B* 87 (2002) 95–98, [https://doi.org/10.1016/S0925-4005\(02\)00224-1](https://doi.org/10.1016/S0925-4005(02)00224-1).
- [2] A. Stambouli Boudghene, E. Traversa, Solid oxide fuel cells (SOFCs): a review of an environmentally clean and efficient source of energy, *Renew. Sustain. Energy Rev.* 6 (2002) 433–455, [https://doi.org/10.1016/S1364-0321\(02\)00014-X](https://doi.org/10.1016/S1364-0321(02)00014-X).
- [3] T. Montini, M. Melchionna, M. Monai, P. Fornasiero, Fundamentals and catalytic applications of CeO<sub>2</sub>-based materials, *Chem. Rev.* 116 (2016) 5987–6041, <https://doi.org/10.1021/acs.chemrev.5b00603>.
- [4] A. Trovarelli, C. de Leitenburg, M. Boaro, G. Dolcetti, The utilization of ceria in industrial catalysis, *Catal. Today* 50 (1999) 353–367, [https://doi.org/10.1016/S0920-5861\(98\)00515-X](https://doi.org/10.1016/S0920-5861(98)00515-X).
- [5] R. Kopelent, J.A. van Bokhoven, J. Szlachetko, J. Edebeli, C. Paun, M. Nachtegaal, et al., Catalytically active and spectator Ce<sup>3+</sup> in ceria-supported metal catalysts, *Angew. Chemie Int. Ed.* 54 (2015) 8728–8731, <https://doi.org/10.1002/anie.201503022>.
- [6] J. Kašpar, P. Fornasiero, M. Graziani, Use of CeO<sub>2</sub>-based oxides in the three-way catalysis, *Catal. Today* 50 (1999) 285–298, [https://doi.org/10.1016/S0920-5861\(98\)00510-0](https://doi.org/10.1016/S0920-5861(98)00510-0).
- [7] Y. Guan, D.A.J.M. Ligthart, Ö. Pirgon-Galin, J.A.Z. Pieterse, R.A. van Santen, E.J.M. Hensen, Gold stabilized by nanostructured ceria supports: nature of the active sites and catalytic performance, *Top. Catal.* 54 (2011) 424–438, <https://doi.org/10.1007/s11244-011-9673-2>.
- [8] K. Zhou, X. Wang, X. Sun, Q. Peng, Y. Li, Enhanced catalytic activity of ceria nanorods with well-defined reactive crystal planes, *J. Catal.* 229 (2005) 206–212, <https://doi.org/10.1016/j.jcat.2004.11.004>.
- [9] E. Aneggi, D. Wiater, C. de Leitenburg, J. Llorca, A. Trovarelli, Shape-dependent activity of ceria in soot combustion, *ACS Catal.* 4 (2014) 172–181, <https://doi.org/10.1021/cs400850r>.
- [10] H.-X. Mai, L.-D. Sun, Y.-W. Zhang, R. Si, W. Feng, H.-P. Zhang, et al., Shape-selective synthesis and oxygen storage behavior of ceria nanopolyhedra, nanorods, and nanocubes, *J. Phys. Chem. B* 109 (2005) 24380–24385, <https://doi.org/10.1021/jp055584b>.
- [11] C. Pan, D. Zhang, L. Shi, J. Fang, Template-Free synthesis, controlled conversion, and CO oxidation properties of CeO<sub>2</sub> nanorods, nanotubes, nanowires, and nanocubes, *Eur. J. Inorg. Chem.* 2008 (2008) 2429–2436, <https://doi.org/10.1002/ejic.200800047>.
- [12] C. Sun, H. Li, H. Zhang, Z. Wang, L. Chen, Controlled synthesis of CeO<sub>2</sub> nanorods by a solvothermal method, *Nanotechnology* 16 (2005) 1454–1463, <https://doi.org/10.1088/0957-4484/16/9/006>.
- [13] W. Song, A.P.J. Jansen, E.J.M. Hensen, A computational study of the influence of the ceria surface termination on the mechanism of CO oxidation of isolated Rh atoms, *Faraday Discuss.* 162 (2013) 281, <https://doi.org/10.1039/c3fd20129e>.
- [14] Y. Jiang, J.B. Adams, M. Van Schilfgaarde, Density-functional calculation of CeO<sub>2</sub> surfaces and prediction of effects of oxygen partial pressure and temperature on stabilities, *J. Chem. Phys.* 123 (2005) 64701, <https://doi.org/10.1063/1.1949189>.
- [15] Z. Wu, M. Li, J. Howe, H.M. Meyer, S.H. Overbury, Probing defect sites on CeO<sub>2</sub> nanocrystals with well-defined surface planes by raman spectroscopy and O<sub>2</sub> adsorption, *Langmuir* 26 (2010) 16595–16606, <https://doi.org/10.1021/la101723w>.
- [16] Z. Ji, X. Wang, H. Zhang, S. Lin, H. Meng, B. Sun, et al., Designed synthesis of CeO<sub>2</sub> nanorods and nanowires for studying toxicological effects of high aspect ratio nanomaterials, *ACS Nano* 6 (2012) 5366–5380, <https://doi.org/10.1021/nn3012114>.
- [17] S. Agarwal, L. Lefferts, B.L. Mojet, D.A.J.M. Ligthart, E.J.M. Hensen, D.R.G. Mitchell, et al., Exposed surfaces on shape-controlled ceria nanoparticles revealed through AC-TEM and water-gas shift reactivity, *ChemSusChem* 6 (2013) 1898–1906, <https://doi.org/10.1002/cssc.201300651>.
- [18] C. Yang, X. Yu, S. Heißler, A. Nefedov, S. Colussi, J. Llorca, et al., Surface faceting and reconstruction of ceria nanoparticles, *Angew. Chemie Int. Ed.* 56 (2017) 375–379, <https://doi.org/10.1002/anie.201609179>.
- [19] B. Murugan, A.V. Ramaswamy, Defect-site promoted surface reorganization in nanocrystalline ceria for the low-temperature activation of ethylbenzene, *J. Am. Chem. Soc.* 129 (2007) 3062–3063, <https://doi.org/10.1021/ja066834k>.
- [20] X. Liu, K. Zhou, L. Wang, B. Wang, Y. Li, Oxygen vacancy clusters promoting reducibility and activity of ceria nanorods, *J. Am. Chem. Soc.* 131 (2009) 3140–3141, <https://doi.org/10.1021/ja808433d>.
- [21] L. Meng, A.P. Jia, J.Q. Lu, L.F. Luo, W.-X. Huang, M.F. Luo, Synergetic effects of PdO species on CO oxidation over PdO-CeO<sub>2</sub> catalysts, *J. Phys. Chem. C* 115 (2011) 19789–19796, <https://doi.org/10.1021/jp2056688>.
- [22] L. Nie, D. Mei, H. Xiong, B. Peng, Z. Ren, X.I.P. Hernandez, et al., Activation of surface lattice oxygen in single-atom Pt/CeO<sub>2</sub> for low-temperature CO oxidation, *Science* 358 (2017) 1419–1423, <https://doi.org/10.1126/science.aao2109>.
- [23] D. Wang, Y. Kang, V. Doan-Nguyen, J. Chen, R. Küngas, N.L. Wieder, et al., Synthesis and oxygen storage capacity of two-dimensional ceria nanocrystals, *Angew. Chemie – Int. Ed.* 50 (2011) 4378–4381, <https://doi.org/10.1002/anie.201101043>.
- [24] J. Stubenrauch, J.M. Vohs, Interaction of CO with Rh supported on stoichiometric and reduced CeO<sub>2</sub> (111) and CeO<sub>2</sub> (100) surfaces, *J. Catal.* 159 (1996) 50–57 (Accessed September 4 2018).
- [25] D.R. Mullins, The surface chemistry of cerium oxide, *Surf. Sci. Rep.* 70 (2015) 42–85, <https://doi.org/10.1016/j.surrep.2014.12.001>.
- [26] J. Jones, H. Xiong, A.T. DeLaRiva, E.J. Peterson, H. Pham, S.R. Challa, et al., Thermally stable single-atom platinum-on-ceria catalysts via atom trapping, *Science* 353 (2016) 150–154, <https://doi.org/10.1126/science.aaf8800>.
- [27] M. Cargnello, J.J. Delgado Jaén, J.C. Hernández Garrido, K. Bakhmutsky, T. Montini, J.J. Calvino Gámez, et al., Exceptional activity for methane combustion over modular Pd@CeO<sub>2</sub> subunits on functionalized Al<sub>2</sub>O<sub>3</sub>, *Science* 337 (2012) 713–717, <https://doi.org/10.1126/science.1222887>.
- [28] J. Wang, H. Chen, Z. Hu, M. Yao, Y. Li, A review on the Pd-based three-way catalyst, *Catal. Rev. Sci. Eng.* 57 (2015) 79–144, <https://doi.org/10.1080/01614940.2014.977059>.
- [29] S. Fouladvand, S. Schernich, J. Libuda, H. Grönbeck, T. Pingel, E. Olsson, et al., Methane oxidation Over Pd supported on Ceria-Alumina under Rich/Lean cycling conditions, *Top. Catal.* 56 (2013) 410–415, <https://doi.org/10.1007/s11244-013-9988-2>.
- [30] L. Xiao, K. Sun, X. Xu, X. Li, Low-temperature catalytic combustion of methane over Pd/CeO<sub>2</sub> prepared by deposition–precipitation method, *Catal. Commun.* 6 (2005) 796–801, <https://doi.org/10.1016/j.catcom.2005.07.015>.
- [31] Y. Zhou, N.J. Lawrence, T.-S. Wu, J. Liu, P. Kent, Y.-L. Soo, et al., Pd/CeO<sub>2</sub>–x nanorod catalysts for CO oxidation: insights into the origin of their regenerative ability at room temperature, *ChemCatChem* 6 (2014) 2937–2946, <https://doi.org/10.1021/cctc.201402243>.
- [32] H. Zhu, Z. Qin, W. Shan, W. Shen, J. Wang, Low-temperature oxidation of CO over Pd/CeO<sub>2</sub>-TiO<sub>2</sub> catalysts with different pretreatments, *J. Catal.* 233 (2005) 41–50, <https://doi.org/10.1016/j.jcat.2005.04.033>.
- [33] M.-F. Luo, Z. Hou, X. Yuan, X.-M. Zheng, Characterization study of CeO<sub>2</sub> supported Pd catalyst for low-temperature carbon monoxide oxidation, *Catal. Lett.* 50 (1998) 205–209, <https://doi.org/10.1023/A:1019023220271>.
- [34] S.-H. Oh, G.B. Hoflund, Chemical state study of palladium powder and ceria-supported palladium during low-temperature CO oxidation, *J. Phys. Chem. A* 110 (2006) 7609–7613, <https://doi.org/10.1021/jp060435u>.
- [35] M. Manzoli, F. Bocuzzi, A. Chiiorio, F. Vindigni, W. Deng, M. Flytzani-Stephanopoulos, Spectroscopic features and reactivity of CO adsorbed on different Au/CeO<sub>2</sub> catalysts, *J. Catal.* 245 (2007) 308–315, <https://doi.org/10.1016/j.jcat.2006.10.021>.
- [36] E.J. Peterson, A.T. DeLaRiva, S. Lin, R.S. Johnson, H. Guo, J.T. Miller, et al., Low-

- temperature carbon monoxide oxidation catalysed by regenerable atomically dispersed palladium on alumina, *Nat. Commun.* 5 (2014) 4885, <https://doi.org/10.1038/ncomms5885>.
- [37] M. Cargnello, V.V.T. Doan-Nguyen, T.R. Gordon, R.E. Diaz, E.A. Stach, R.J. Gorte, et al., Control of metal nanocrystal size reveals metal-support interface role for ceria catalysts, *Science* 341 (2013) 771–773, <https://doi.org/10.1126/science.1240148>.
- [38] R. Si, M. Flytzani-Stephanopoulos, Shape and crystal-plane effects of nanoscale ceria on the activity of Au-CeO<sub>2</sub> catalysts for the water-gas shift reaction, *Angew. Chemie – Int. Ed.* 47 (2008) 2884–2887, <https://doi.org/10.1002/anie.200705828>.
- [39] R. Peng, X. Sun, S. Li, L. Chen, M. Fu, J. Wu, et al., Shape effect of Pt/CeO<sub>2</sub> catalysts on the catalytic oxidation of toluene, *Chem. Eng. J.* 306 (2016) 1234–1246, <https://doi.org/10.1016/j.cej.2016.08.056>.
- [40] L. Soler, A. Casanovas, A. Urrich, I. Angurell, J. Llorca, CO oxidation and COPrOx over preformed Au nanoparticles supported over nanoshaped CeO<sub>2</sub>, *Appl. Catal. B Environ.* 197 (2016) 47–55, <https://doi.org/10.1016/j.apcatb.2016.02.025>.
- [41] G. Spezzati, Y. Su, J.P. Hofmann, A.D. Benavidez, A.T. Delariva, J. McCabe, et al., Atomically dispersed Pd-O species on CeO<sub>2</sub>(111) as highly active sites for low-temperature CO oxidation, *ACS Catal.* 7 (2017) 6887–6891, <https://doi.org/10.1021/acscatal.7b02001>.
- [42] B. Ravel, M. Newville, ATHENA, ARTEMIS, HEPHAESTUS: data analysis for X-ray absorption spectroscopy using IFEFFIT, *J. Synchrotron Radiat.* 12 (2005) 537–541, <https://doi.org/10.1107/S0909049505012719>.
- [43] J.P. Perdew, K. Burke, M. Ernzerhof, Generalized gradient approximation made simple, *Phys. Rev. Lett.* 77 (1996) 3865–3868, <https://doi.org/10.1103/PhysRevLett.77.3865>.
- [44] G. Kresse, J. Furthmüller, Efficient iterative schemes for ab initio total-energy calculations using a plane-wave basis set, *Phys. Rev. B* 54 (1996) 11169–11186, <https://doi.org/10.1103/PhysRevB.54.11169>.
- [45] G. Kresse, J. Furthmüller, Efficiency of ab-initio total energy calculations for metals and semiconductors using a plane-wave basis set, *Comput. Mater. Sci.* 6 (1996) 15–50, [https://doi.org/10.1016/0927-0256\(96\)00008-0](https://doi.org/10.1016/0927-0256(96)00008-0).
- [46] S.L. Dudarev, G.A. Botton, S.Y. Savrasov, C.J. Humphreys, a.P. Sutton, Electron-energy-loss spectra and the structural stability of nickel oxide: an LSDA + U study, *Phys. Rev. B* 57 (1998) 1505–1509, <https://doi.org/10.1103/PhysRevB.57.1505>.
- [47] P.E. Blöchl, Projector augmented-wave method, *Phys. Rev. B* 50 (1994) 17953–17979, <https://doi.org/10.1103/PhysRevB.50.17953>.
- [48] G. Kresse, D. Joubert, From ultrasoft pseudopotentials to the projector augmented-wave method, *Phys. Rev. B* 59 (1999) 1758–1775, <https://doi.org/10.1103/PhysRevB.59.1758>.
- [49] S. Fabris, S. De Gironcoli, S. Baroni, G. Vicario, G. Balducci, Taming multiple valency with density functionals: a case study of defective ceria, *Phys. Rev. B* 71 (2005), [https://doi.org/10.1103/PhysRevB.71.041102\(R\)](https://doi.org/10.1103/PhysRevB.71.041102).
- [50] M. Cococcioni, S. De Gironcoli, Linear response approach to the calculation of the effective interaction parameters in the LDA + U method, *Phys. Rev. B* 71 (2005) 035105–035121, <https://doi.org/10.1103/PhysRevB.71.035105>.
- [51] C.W.M. Castleton, J. Kullgren, K. Hermansson, Tuning LDA + U for electron localization and structure at oxygen vacancies in ceria, *J. Chem. Phys.* 127 (2007) 244704–244715.
- [52] J.L.F. Da Silva, M.V. Ganduglia-Pirovano, J. Sauer, V. Bayer, G. Kresse, Hybrid functionals applied to rare-earth oxides: the example of ceria, *Phys. Rev. B – Condens. Matter Mater. Phys.* 75 (2007) 045121–045131, <https://doi.org/10.1103/PhysRevB.75.045121>.
- [53] G. Henkelman, B.P. Uberuaga, H. Jónsson, Climbing image nudged elastic band method for finding saddle points and minimum energy paths, *J. Chem. Phys.* 113 (2000) 9901–9904, <https://doi.org/10.1063/1.1329672>.
- [54] D. Porezag, M.R. Pederson, Infrared intensities and raman-scattering activities within density-functional theory, *Phys. Rev. B – Condens. Matter Mater. Phys.* 54 (1996) 7830–7836, <https://doi.org/10.1103/PhysRevB.54.7830>.
- [55] I.A.W. Filot, R.A. van Santen, E.J.M. Hensen, The optimally performing Fischer – Tropsch catalyst, *Angew. Chemie* 126 (2014) 12746–12750, <https://doi.org/10.1002/anie.201406521>.
- [56] I.A.W. Filot, R.J.P. Broos, J.P.M. Van Rijn, G.J.H.A. Van Heugten, R.A. van Santen, E.J.M. Hensen, First-principles-based microkinetics simulations of synthesis gas conversion on a stepped rhodium surface, *ACS Catal.* 5 (2015) 5453–5467, <https://doi.org/10.1021/acscatal.5b01391>.
- [57] H. Eyring, The activated complex in chemical reactions, *J. Chem. Phys.* 3 (1935) 107–115, <https://doi.org/10.1063/1.1749604>.
- [58] P. Nitoń, A. Źywociński, M. Fiałkowski, R. Holyst, A “nano-windmill” driven by a flux of water vapour: a comparison to the rotating ATPase, *Nanoscale* 5 (2013) 9732, <https://doi.org/10.1039/c3nr03496h>.
- [59] Filot, I.A.W., Zijlstra, B., Hensen, E.J.M. MKMCXX, a C + program for constructing microkinetic models., (n.d.). <https://www.mkmcxx.nl/> (Accessed May 1, 2018).
- [60] C.T. Campbell, Future directions and industrial perspectives micro- and macro-kinetics: their relationship in heterogeneous catalysis, *Top. Catal.* 1 (1994) 353–366, <https://doi.org/10.1007/BF01492288>.
- [61] C.T. Campbell, Finding the rate-determining step in a mechanism: comparing DeDonder relations with the “Degree of rate control, *J. Catal.* 204 (2001) 520–524, <https://doi.org/10.1006/jcat.2001.3396>.
- [62] C. Stegemann, A. Andreassen, C.T. Campbell, Degree of rate control: how much the energies of intermediates and transition states control rates, *J. Am. Chem. Soc.* 131 (2009) 8077–8082, <https://doi.org/10.1021/ja9000097>.
- [63] S. Agarwal, X. Zhu, E.J.M. Hensen, L. Lefferts, B.L. Mojet, Defect chemistry of ceria nanorods, *J. Phys. Chem. C* 118 (2014) 4131–4142, <https://doi.org/10.1021/jp409989y>.
- [64] Z. Hu, X. Liu, D. Meng, Y. Guo, Y. Guo, G. Lu, Effect of ceria crystal plane on the physicochemical and catalytic properties of Pd/ceria for CO and propane oxidation, *ACS Catal.* 6 (2016) 2265–2279, <https://doi.org/10.1021/acscatal.5b02617>.
- [65] Y.Q. Su, I.A.W. Filot, J.X. Liu, E.J.M. Hensen, Stable Pd-doped ceria structures for CH<sub>4</sub> activation and CO oxidation, *ACS Catal.* 8 (2018) 75–80, <https://doi.org/10.1021/acscatal.7b03295>.
- [66] W. Song, C. Popa, A.P.J. Jansen, E.J.M. Hensen, Formation of a rhodium surface oxide film in Rh n/CeO<sub>2</sub>(111) relevant for catalytic CO oxidation : a computational study, *J. Phys. Chem. C* 116 (2012) 22904–22915, <https://doi.org/10.1021/jp306863d>.
- [67] M. Nolan, S.C. Parker, G.W. Watson, The electronic structure of oxygen vacancy defects at the low index surfaces of ceria, *Surf. Sci.* 595 (2005) 223–232, <https://doi.org/10.1016/j.susc.2005.08.015>.
- [68] C. Binet, A. Badri, J.-C. Lavalley, A spectroscopic characterization of the reduction of ceria from electronic transitions of intrinsic point defects, *J. Phys. Chem.* 98 (1994) 6392–6398, <https://doi.org/10.1021/j100076a025>.
- [69] G.C. Cabilla, A. Bonivardi, M. Baltanas, Characterization by CO/FTIR spectroscopy of Pd/silica catalysts and its correlation with syn-gas conversion, *Catal. Lett.* 55 (1998) 147–156, <https://doi.org/10.1023/A:1019095231484>.
- [70] J. Nilsson, P.-A. Carlsson, S. Fouladvand, N.M. Martin, J. Gustafson, Ma. Newton, et al., Chemistry of supported palladium nanoparticles during methane oxidation, *ACS Catal.* (2015) 2481–2489, <https://doi.org/10.1021/cs502036d>.